



Catalytic activity of laundering durable fiber-based manganese dioxide catalyst targeting indoor formaldehyde

Zijian Duan ^{a,1}, Yahui Zhou ^{a,1}, Huiyu Yang ^{b,1}, Dali Yan ^a, Dengpeng Song ^a, Hao Liu ^c, Bo Deng ^{a,*}, Shuai Peng ^{a,d,*}, Weilin Xu ^{a,*}

^a State Key Laboratory of New Textile Materials and Advanced Processing Technologies, Hubei Provincial Engineering Laboratory for Clean Production and High Value Utilization of Bio-Based Textile Materials, Wuhan Textile University, Wuhan 430200, China

^b College of Chemistry and Materials Science, Hubei Engineering University, Xiaogan 43200, China

^c State Key Laboratory of Coal Combustion, Huazhong University of Science and Technology, Wuhan 430074, China

^d College of Life Science, South-Central MinZu University, Wuhan 430074, China



ARTICLE INFO

Keywords:

$\delta\text{-MnO}_2$
Formaldehyde
Oxygen vacancy
Laundering durability

ABSTRACT

Fiber-based MnO_2 nanocatalysts show high practical potential for their easy recovery. While significantly reducing specific surface area, catalytic performance, and poor laundering durability hinder their further applications for formaldehyde removal. Here, surface $-\text{OH}$ and $-\text{COOH}$ on PMIA were finely regulated by varying the plasma treatment durations. $-\text{OH}$ plays as a reduction agent to facilitate the production of Mn^{3+} close to the PMIA surface and thus promote subsequent output of oxygen vacancy (OV). The plasma introduced and $-\text{OH}$ oxidized $-\text{COOH}$ acted together as multiple binding sites to bridge the MnO_2 catalyst and PMIA fiber, which endows the $\text{MnO}_2@\text{PMIA}$ excellent laundering durability evidenced by the almost unchanged catalytic performance targeting formaldehyde even after 20 home laundering cycles. The mechanism of modulation of oxygen vacancy and specific surface area and water fastness by *in situ* $-\text{OH}$ and $-\text{COOH}$ on the relevant surfaces is proposed and confirmed by FTIR, XPS, SEM, and BET. $\text{MnO}_2@\text{PMIA-6}$ demonstrated the highest catalytic activity for the degradation of formaldehyde, up to 95.43 % in 1 h at room temperature. The catalytic activity remained at 90.97 % with only 0.94 % loss of catalyst mass after 20 home laundering cycles.

1. Introduction

Modern home furnishing materials emit volatile organic compounds (VOCs), which can cause health hazards such as headaches, nausea, vomiting, and weakness in the limbs [1–3]. Furthermore, prolonged exposure to high levels of VOCs can damage the sensory nerves, leading to severe symptoms such as convulsions, coma, and memory loss [4,5]. One of the most common VOCs is formaldehyde (HCHO), which has been linked to multiple leukemias in infants [6]. High concentrations of HCHO in the environment can lead to the rapid development of leukemia [7–9]. As a result, many people are interested in finding safe and effective ways to degrade HCHO.

Recent studies have discovered that various transition metal oxides, such as MnO_2 , TiO_2 , Co_3O_4 , and CeO_2 , have shown promising catalytic degradation properties for formaldehyde [10–12]. Nano- MnO_2 has

emerged as the most efficient catalyst for this process [13–15]. The unique layered structure of $\delta\text{-MnO}_2$, which exists in nature in the form of $[\text{MnO}_6]$ n-octahedra, distinguishes it from other crystalline forms of MnO_2 [16,17]. The exposed catalytically active sites on the surface of $\delta\text{-MnO}_2$ are responsible for its superior catalytic degradation performance, which can be achieved even at room temperature without light [18–20].

Furthermore, studies have shown that precise regulation of oxygen vacancies (OV) in $\delta\text{-MnO}_2$ can significantly influence the electronic structure of the catalyst surface. This, in turn, enhances electron enrichment, facilitating the adsorption of reactive oxygen species and ultimately boosting the catalytic performance of nano $\delta\text{-MnO}_2$ [21–23].

While the inevitable agglomeration of $\delta\text{-MnO}_2$ nanoparticles makes the catalytic activity decay sharply, as well as the difficult recycling properties, which are harmful to the environment and human health

* Corresponding authors at: State Key Laboratory of New Textile Materials and Advanced Processing Technologies, Hubei Provincial Engineering Laboratory for Clean Production and High Value Utilization of Bio-Based Textile Materials, Wuhan Textile University, Wuhan 430200, China.

E-mail addresses: dengjianguo88@outlook.com (B. Deng), gwpzs211@wtu.edu.cn (S. Peng), weilin-xu@hotmail.com (W. Xu).

¹ Zijian Duan, Yahui Zhou, and Huiyu Yang contributed equally to this work.

when left in the natural environment, making it difficult to apply directly [24,25]. Dispersed loading of nano-MnO₂ onto fiber can combine adsorption, non-agglomeration, high catalytic, easy recycling, and green properties. In addition, the soft and breathable nature of fiber makes it suitable for air purification equipment and various shaped mechanical devices that require high-velocity airflow, making fiber-based nano-MnO₂ catalysts more widely used in industry and everyday life than nano-MnO₂ catalysts. Thus, the research on the mechanism and product development of fiber-based nano-MnO₂ catalysts has important scientific value and application prospects.

Currently, the simplest and most effective method for loading nano δ-MnO₂ catalysts on fiber is the hydrothermal synthesis method. However, the inevitable significant decrease in the specific surface area of the MnO₂ catalytic layer after fiber loading leads to a significant attenuation of the catalytic activity, which becomes one of the key bottlenecks preventing its practical application [26].

Zijian Dai et al. reported for the first time that the microscopic morphology of MnO₂ nanoparticles could be adjusted by modulating the type of metal oxide seed layer on the fiber surface, thereby modulating the specific surface area, resulting in a significant increase in the catalytic activity of fiber-based MnO₂ nanoparticles [27]. The catalytic activity of fiber-based MnO₂ catalysts was significantly improved. This study provides a new idea and theoretical basis for the use of surface chemistry to regulate the structure and performance of hydrothermally synthesized fiber-based MnO₂ catalysts.

One of the bottlenecks preventing the practical application of fiber-based MnO₂ nanocatalysts is the low concentration of OV in the MnO₂ catalyst layer, resulting in low catalytic activity [28].

Mainstream research in this field has shown that the concentration of OV in the MnO₂ catalyst layer can be increased by adding free reducing agents (ammonia, ammonium oxalate, glucose, methanol, etc. [29–31]) to the hydrothermal solution to generate Mn³⁺ to up-regulate the OV in the nano-MnO₂ (the presence of Mn³⁺ causes the charge in the [MnO₆] octahedra to be out of balance, resulting in the formation of OV when the O atoms in the lattice are detached) [32].

However, most of the free reducing agent is free in solution and only a small fraction can react in contact with the fiber (Fig. 1). As a result, most of the Mn³⁺ produced is combined with the freely growing [MnO₆] in solution, resulting in a limited increase in the OV content of the fiber-based MnO₂ layer, and there is still room for further improvement in catalytic activity. If the production of Mn³⁺ can be restricted to the near surface of the fiber employing fiber-specific surface functional groups such as hydroxyl groups, the fiber-based MnO₂ catalytic layer can be made to contain a higher relative concentration of OV, resulting in a higher catalytic activity than the free reductant approach [33]. Here the OV was produced outside near the MnO_x side.

Existing studies to improve the activity of fiber-based MnO₂ catalysts usually use a single isolated means of modulating the specific surface area [34] or OV [35], but no reports have been seen on the use of both strategies to improve the activity of fiber-based MnO₂ catalysts. It is

believed that the synergistic use of both strategies will further enhance the catalytic activity of fiber-based MnO₂ nanocatalysts and make them more practical.

The lack of chemical bonding between the fiber and the MnO₂ layer leads to MnO₂ layers peeling off after washing and a drastic decay of the catalytic performance, which becomes the third key bottleneck preventing the practical application of fiber-based MnO₂ nanocatalysts.

For all functional fibers, including superhydrophobic [36], structured colors [37], and antibacterial fiber [38], the washing resistance for a specific function is a key factor in determining its service life. The better the washing resistance, the more times a functional fiber can be reused and the lower its cost of use, which is more conducive to its practical application [39]. Recyclability and maintaining high catalytic activity after recycling are key issues that have long existed in the practical application of fiber-based MnO₂ nanocatalysts.

Although fiber-based MnO₂ nanocatalysts can be regenerated for catalytic function after a simple heat treatment, they still need to be washed to remove impurities such as solid dust from the surface to maintain good catalytic activity in practical industrial and domestic applications. In addition, if fiber-based MnO₂ nanocatalysts can be given excellent washing resistance properties, they can be further used in high-value-added functional textiles such as formaldehyde removal curtains and formaldehyde removal garments. Unfortunately, there is still a lack of effective means of constructing chemical bonding between the inorganic MnO₂ catalytic layer and organic fiber in hydrothermal reactions. Therefore, the mainstream studies of fiber-based MnO₂ nanocatalysts have not yet seen reports of their catalytic activity for washing resistance properties. We have reason to believe that this is one of the key bottlenecks limiting the practical application of fiber-based MnO₂ nanocatalysts.

In conclusion, the three main challenges to realizing real practical applications of fiber-based MnO₂ nanocatalysts are the reduced specific surface area of the active ingredient, the low concentration of OV, and the lack of chemical bonding between the MnO₂ layer and the fiber. A strategy to chemically bond inorganic MnO₂ layers to organic fibers while up-regulating the specific surface area and oxygen vacancy concentration of MnO₂ nanocatalysts is urgently needed for the practical application of fiber-based MnO₂ nanocatalysts.

To address the three major challenges facing the practical application of fiber-based MnO₂ nanocatalysts, we used plasma for the first time to synchronize the controlled production of hydroxyl and carboxyl groups on the surface of Poly-m-phenylene isophthalamide 1313 (PMIA).

The hydrothermal reaction occurs in a closed, high-temperature, high-pressure, strongly oxidizing environment. The choice of PMIA, a fabric with excellent heat and corrosion resistance, can effectively avoid its breakage during the hydrothermal process. In the subsequent hydrothermal synthesis, the content and distribution of carboxyl groups on the fiber surface determine the content and distribution of the adsorbed Mn active species, and the morphology of the hydrothermally grown MnO₂ nanoparticles is effectively regulated by changing the number of nuclei, which in turn regulates their specific surface area. Weakly reducing -OH (non-solution-free reducing agents) on the fiber surface generates abundant Mn³⁺ near the fiber surface in a fixed domain. These Mn³⁺ are encapsulated by the MnO₂ crystals growing near the fiber surface, resulting in a fiber-based MnO₂ catalyst with a high oxygen vacancy concentration. At the same time, the carboxyl groups on the surface of the PMIA after plasma treatment can act as chemical bonding functional groups to anchor the MnO₂ nanocrystals to the PMIA fiber, which is expected to give the fiber-based MnO₂ catalyst better resistance to washing (Fig. 2).

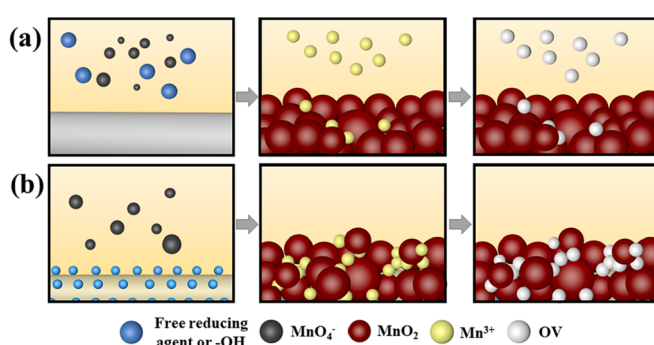


Fig. 1. Mechanism of the effect of (a) free -OH, (b) in situ -OH on the OV concentration on the surface of PMIA.

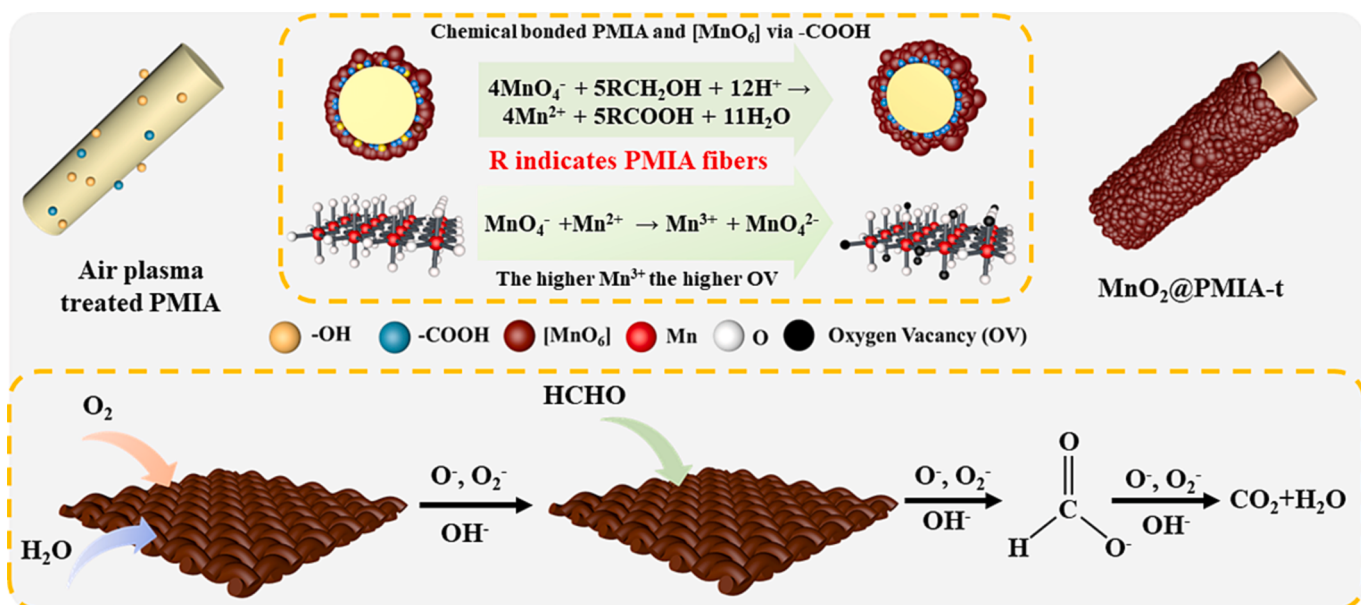


Fig. 2. Systematic modulation of the specific surface area, catalytic activity, and laundering durability of fiber-based MnO_2 nanocatalysts.

2. Experimental

2.1. Chemicals

Potassium permanganate (>99.5 , KMnO_4) was purchased from Tianjin Tianda Chemical Reagent Factor. Poly-m-phenylene isophthalamide 1313 (40 g/m², PMIA) was purchased from Tayho. Anhydrous ethanol (AR), Formaldehyde solution (AR, contains 37.0 ~ 40.0 % HCHO and 8%~14 % CH_3OH as a stabilizer), Vitamin B₆ (99 %, $\text{C}_8\text{H}_{11}\text{NO}_3\text{HCl}$), and Sodium hypochlorite (CP, NaClO) were purchased from Sinopharm Chemical Reagent Co., Ltd. American Association of Textile Chemists and Colorists (AATCC) standard WOB detergent was purchased from Shanghai Pinkui Electromechanical Technology Co., Ltd.

2.2. Synthesis of MnO_2 @PMIA

2.2.1. Synthesis of MnO_2 @PMIA-t

Each PMIA fabric (30 mm × 60 mm, 40 g/m²) was placed in a plasma cleaner (PDC-002, Harrick, USA). Both sides of the PMIA cloth were treated with air plasma at 1 Torr for 2, 4, 6, 8, and 10 min. The resulting samples were named PMIA-t (t = plasma treatment durations).

1.80 g KMnO_4 was dissolved in 100 mL of deionized water and stirred in a magnetic stirrer at 200 r/min for 15 min until the KMnO_4 is completely dissolved. The plasma-cleaned PMIA cloth was immersed in this solution, stirred continuously for 30 min, and then transferred to the PTFE liner. The Teflon liner was placed in a hydrothermal kettle and sealed, then transferred to a hydrothermal chamber (PRD-C3000, Shanghai Suopu Instrument Co., Ltd, China). The reactor was heated from room temperature to 90 °C at a rate of 10 °C/min and then kept for 10 h. The product was washed three times with deionized water followed by anhydrous ethanol and then air dried at room temperature. The resulting sample was named MnO_2 @PMIA-t.

2.2.2. Synthesis of MnO_2 @PMIA-B

To compare the relative amount of OV obtained using -OH free in solution with that of using surface anchored -OH, a control sample named MnO_2 @PMIA-B was prepared according to the following procedure.

0.28 g of vitamin B₆ and 1.80 g of KMnO_4 were dissolved in 50 mL of deionized water, respectively. The PMIA cloth was completely immersed

in the vitamin solution during the stirring process. After stirring, Vitamin B₆ and KMnO_4 solution were mixed, and conduct a hydrothermal reaction. The duration of the hydrothermal reaction is 12 h, and other experimental operations and conditions are the same as 2.2.1. The resulting sample was named MnO_2 @PMIA-B.

2.3. Catalytic performance evaluated by formaldehyde removal

The formaldehyde degradation experiments were performed in a homemade apparatus (Fig. S1). MnO_2 @PMIA-t filter cloth was placed in a glass tube between the reaction vessel and the sensor. At room temperature, 20 mL of Formaldehyde solution was added to a glass gas volatilization device. Formaldehyde mixed with air (relative humidity of 55%, 380 ppm CO_2) was pushed into the reaction vessel by an air pump. Transmission stops when the formaldehyde concentration in the device reaches 100 ppm (135 ppm gaseous methanol). The FTIR gas analyzer (DX4015, Gasmet Technologies Oy) was used to analyze the concentration of HCHO and CO_2 , and flow was achieved within the device ($\text{GHSV} \sim 60000 \text{ mL} \cdot \text{h}^{-1} \cdot \text{g}^{-1}$). The reaction lasted for 1 h. The regeneration of the catalyst is completed by holding it at 110 °C in an air oven for 2 h.

2.4. Laundering durability test

Laundering durability performance was evaluated according to the AATCC Test Method 61-2003 on a standard colorfastness to washing laundering machine (Model SW-12A, Changzhou Dahua Electronic Instrument Co., Ltd. China) equipped with 500 mL (75 mm × 125 mm) stainless-steel lever-lock canisters. The fabric was laundered in a rotating sealed canister containing 150 mL aqueous solution consisting of AATCC standard WOB detergent and 50 stainless steel balls using 5A condition with active chlorine (0.027%, w/w) in a thermostatically controlled water bath at 49 °C, 40 ± 2 rpm. After washed by laundering machine, a home laundering using pure water was further performed to ensure the completely remove of detergent.

The sizes of the fabric samples were 30 mm × 60 mm for each test.

2.5. Characterization

Infrared spectra of the PMIA fiber were recorded using a Fourier transform infrared spectroscope (FTIR, Thermo Scientific iS 50, USA) at

room temperature in the range of 500–4000 cm⁻¹. Thirty-two scans with 4.0 cm⁻¹ resolution were carried out for each case under the reflection mode.

X-ray diffraction (XRD, Empyrean, PANalytical, Germany) analyses were performed on a Cu-K α radiation source. Voltage and current are 40 kV and 50 mA respectively. The sample is scanned at a rate of 5°/min over a range of 10–90°.

Scanning electron microscopy (SEM) and Energy dispersive X-ray spectroscopy (EDX) were obtained on a scanning electron microscope (TESCAN MIRA LMS, Czech).

The samples were pretreated under vacuum at 105 °C for 8 h. The samples were then subjected to N₂ adsorption and desorption tests using a fully automated specific surface area analyzer (Micromeritics ASAP 2460, USA) under 77 k liquid nitrogen to obtain N₂ isothermal adsorption and desorption curves.

Thermogravimetry (TG) and Differential scanning calorimetry (DSC) analysis were performed using a synchronous thermal analyzer (STA8000, PE, USA) with a heating rate of 20 °C min⁻¹ from 30 °C to 800 °C in O₂ gas (20 mL/min).

The chemical states of the catalyst surface elements were examined by X-ray photoelectron spectroscopy (XPS, Thermo Scientific ESCALAB 250Xi, USA) at pass energy of 50 eV, equipped with Al K α as an exciting X-ray source. Binding energies were corrected for surface charging by referring to the energy of the C 1 s peak at 284.8 eV.

The electron paramagnetic resonance (EPR) spectra were obtained by a spectrometer (Bruker EMX PLUS, Germany). Scanning in the range of 3460–3560 G at a modulation frequency of 100 kHz at 295 K.

The H₂-TPR pattern was obtained using a temperature-programmed chemisorption instrument (Microtec BEL Cat II, Japan). The sample was pretreated by drying at a temperature programmed from room temperature to 300 °C at 10 °C/min. He gas flow (50 mL/min) was purged for 1 h, cooled to 50 °C, and a 10% H₂/Ar mixture (50 mL/min) was continuously introduced for 0.5 h. After the baseline is stabilized, the sample is desorbed in a 10% H₂/Ar gas stream at a temperature rise rate of 10 °C/min to 450 °C, and the reducing gas is detected using a thermal

conductivity detector (TCD).

3. Results and discussion

3.1. Construction of –OH and –COOH on the surface of PMIA fibers

Plasma particles (electrons, ions, reactive particles, and UV light, etc.) interact with the fiber surface to break weak bonds (H-C, H-O, H-N, and C-C, etc.) in the macromolecules and replace them with groups (carboxyl, hydroxyl, carbonyl, etc.) in the plasma. At the same time, the etching effect of plasma on the fiber surface makes the fiber surface rough and there is a breakage of chemical bonds and the formation of free radicals [40–42]. We investigated the regulation of hydroxyl and carboxyl groups on the surface of PMIA by infrared spectroscopy at different plasma treatment durations.

Fig. 3a and b gives the FTIR spectra of PMIA samples of different lengths treated under air plasma at 1 T. Infrared spectra of untreated PMIA fibers show a broad peak at 3380–3120 cm⁻¹ attributed to the N-H stretching vibration of the amide bond [43,44].

The number of oxygen-containing functional groups on its surface after plasma treatment is negligible compared to the huge amount of N-H in the PMIA repeating units [45]. Therefore, we normalized the FTIR spectra of all samples using the characteristic peak of N-H at 3300 cm⁻¹ as a reference.

It can be observed that all samples in Fig. 3a show –OH absorption peaks from 3720 to 3620 cm⁻¹ [46] and the peak height increases with increasing plasma treatment time.

Fig. 3c shows the increased integrated area of the –OH characteristic peak with increased plasma treatment time, indicating that the –OH content of the PMIA surface can be effectively regulated by varying the plasma treatment time.

The peak at 1710–1625 cm⁻¹ (Fig. 3b) was attributed to C = O stretching [47] and again the peak area was significantly enhanced with plasma treatment. It is important to note that the pristine PMIA showed significant C = O stretching which is majorly due to the amide groups of

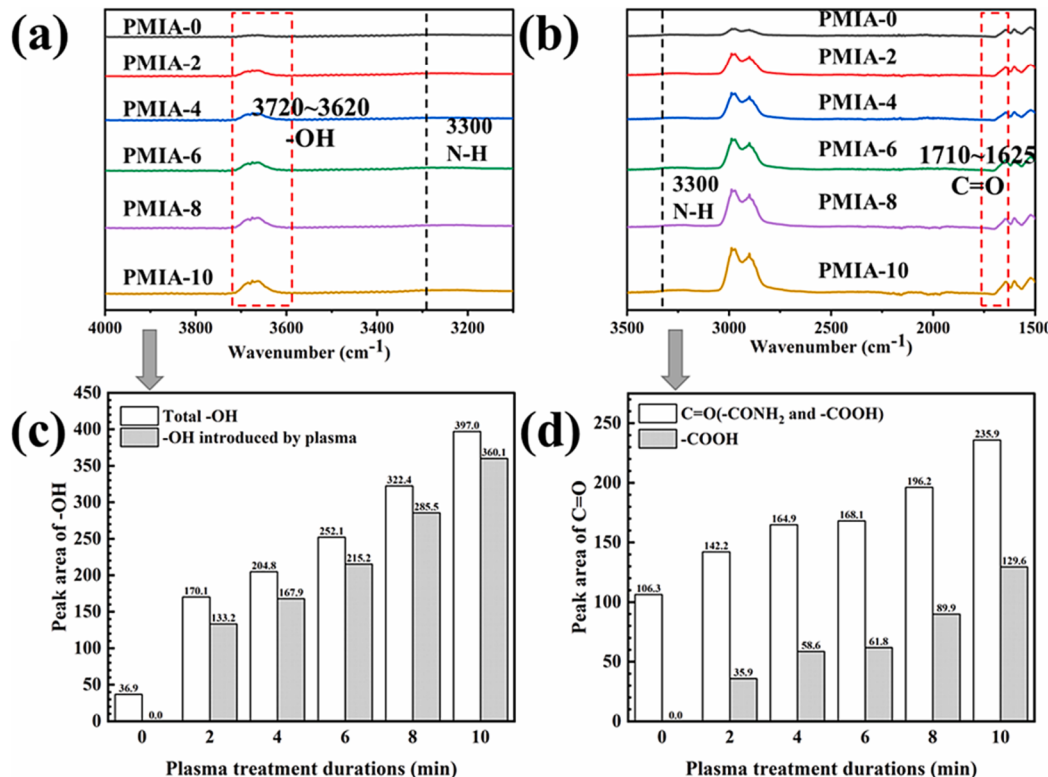


Fig. 3. FTIR spectra of PMIA fibers treated by plasma under different durations (a) –OH, (b) -C=O, The vibration peak area of (c) –OH, (d) C=O.

PMIA. To exclude the contribution of C = O stretching from amide groups, all integration peak area of samples in Fig. 3d was subtracted by the corresponding integration peak area of control PMIA (with shadow). Increased integration neat peak area of –COOH indicating an increase in the concentration of surface –COOH in the sample after extended plasma treatment.

In summary, the regulation of –OH and –COOH on the PMIA surface can be achieved simultaneously by modulating the plasma treatment time.

3.2. Modulation of surface morphology and specific surface area of MnO₂@PMIA

Loading the MnO₂ nanocatalysts onto fiber substrates can effectively facilitate their recovery and reduce their environmental toxicity [18]. While a significant decrease in the specific surface area resulted in the weakened catalytic activity of MnO₂ nanocatalysts. Except for the modulation of OV, the morphology of MnO₂ nanocatalysts which is tightly linked with their specific surface area should be optimized to get the best comprehensive performance of MnO₂ nanocatalysts.

To investigate the effect of surface hydroxyl and carboxyl functional groups on the microscopic morphology of MnO₂ on PMIA surfaces, we used SEM (Fig. 4a-f and Fig. S4a) to demonstrate the evolution of MnO₂ nanoparticles on fiber surfaces with different plasma treatment durations.

In the case of plasma treatment duration of less than 2 min (Fig. 4a and b), the surface of MnO₂ nanoparticles was very sparse and the size of MnO₂ nanoparticles was large. This is due to the small number of active hydroxyl and carboxyl groups on the fiber surface, which do not provide sufficient attachment sites for the free manganese species in the solution. The fiber surface is less bound to MnO₂ and the growth pattern of MnO₂ tends to be more toward free growth in solution.

The –OH and –COOH concentration of the fiber surfaces treated with plasma for 4 and 6 min was moderate, providing a sufficient seed layer for crystal growth without causing the nanoparticles to grow too rapidly. These two samples yielded densely distributed and small-sized MnO₂

nanoparticles, mostly spherical with an average size of 141 and 131 nm respectively (Fig. 4c-d).

When the plasma treatment time was increased to 8 min (Fig. 4e), individual nanoparticles of MnO₂ were easily connected and formed larger size nanoparticles due to the excessive number of active sites in the sample. The overall tendency is towards a transformation from nanoparticles to coatings.

The sample with a plasma treatment time of 10 min (Fig. 4f) was more heavily coated and also had the largest surface nanoparticle size with an average size of 305 nm. The statistically averaged sizes of all nanoparticles were shown in Fig. S2.

SEM images demonstrate that the content of –OH on the surface of PMIA fibers can directly influence the growth morphology of MnO₂ nanoparticles. The microscopic morphology of PMIA fiber-based MnO₂ nanocatalysts can be effectively regulated by plasma treatment time modulation.

Further EDS results for MnO₂@PMIA-6 are provided in Fig. 4g. In addition to the elements C, N, O, and Mn, the element K is also present (Fig. S3). It has been reported in the literature that the presence of K⁺ increases the stability of the δ-MnO₂ interlayer structure and makes it less likely to collapse [48,49].

We further characterized the crystalline form of MnO₂ on PMIA fiber using XRD. The XRD patterns in Fig. 4h show that all samples show diffraction peaks at 12.53°, 23.78°, 37.10°, and 65.92°. Three of the diffraction peaks are consistent with the positions of the standard card (JCPDS 80–1098) for the (001), (–111), and (020) crystal planes of δ-MnO₂, which identifies the sample crystalline type as δ-MnO₂. The XRD spectrum of PMIA showed in Fig. S4b.

To clarify the pattern of the effect of plasma treatment time on the specific surface area of nano-MnO₂, we tested the N₂ adsorption–desorption isotherms of different samples at 77 K using the BET method (Fig. 5a-c).

The specific surface areas determined were 2.46, 8.74, and 7.84 m²/g for the plasma treatment period of 2, 6, and 10 min, respectively (Fig. 5d). All samples were isothermally depressed and showed no inflection points, exhibiting a type III isotherm. the interaction between

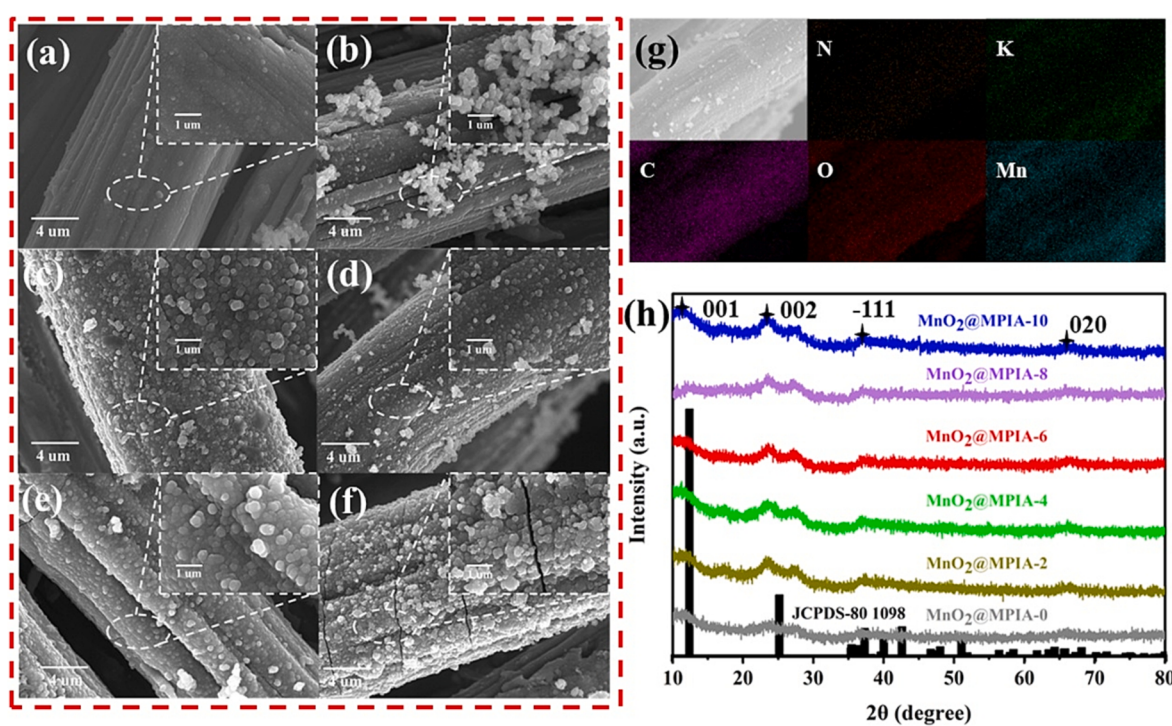


Fig. 4. SEM images of (a) MnO₂@PMIA-0, (b) MnO₂@PMIA-2, (c) MnO₂@PMIA-4, (d) MnO₂@PMIA-6, (e) MnO₂@PMIA-8, (f) MnO₂@PMIA-10, (g) High-resolution EDS mapping images of MnO₂@PMIA-6, (h) XRD patterns of different samples.

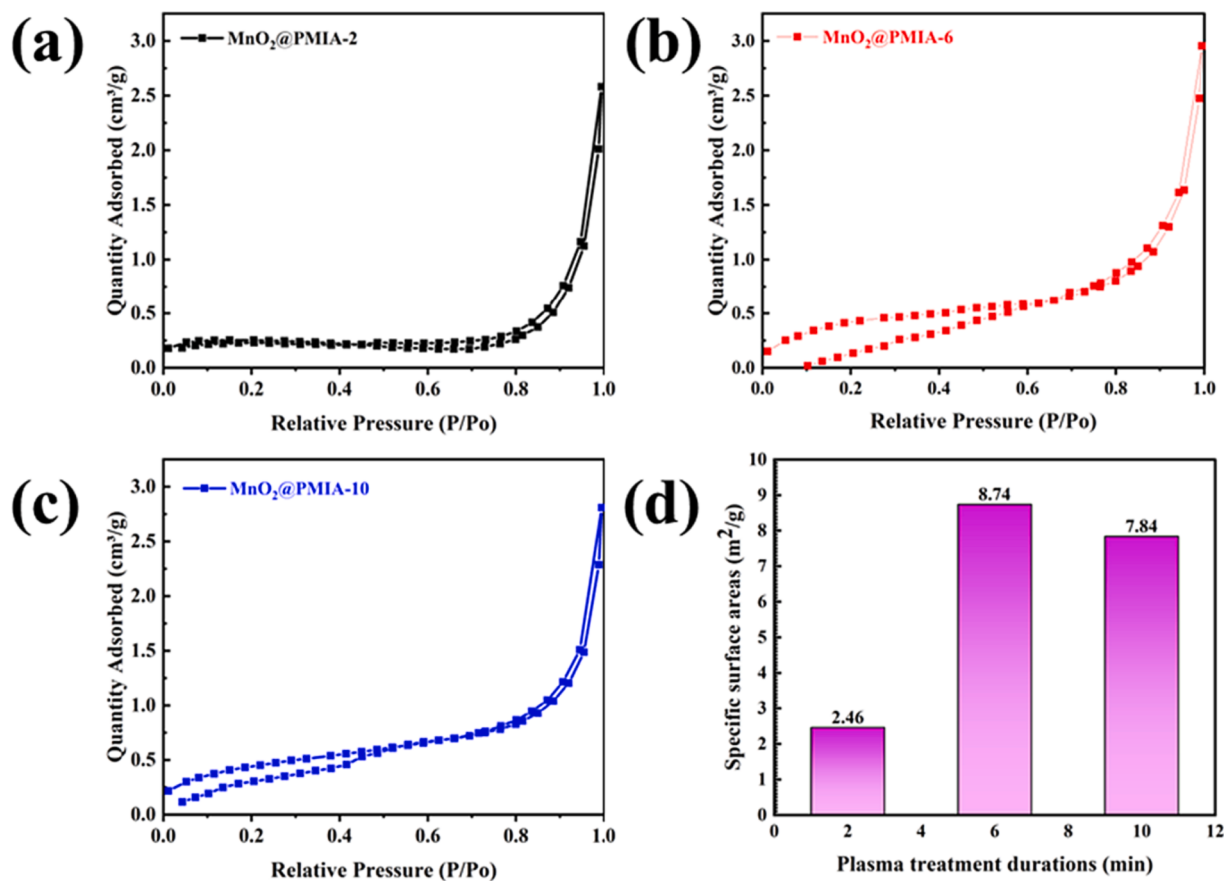


Fig. 5. N₂ isotherms of (a) MnO₂@PMIA-2, (b) MnO₂@PMIA-6, (c) MnO₂@PMIA-10 at 77 K, and (d) corresponding specific surface areas.

the PMIA sample surface and N₂ was weak and the adsorbed N₂ was mainly aggregated by the strongly gravitating MnO₂ nanoparticles.

The MnO₂@PMIA-2 surface has the sparsest MnO₂ nanoparticles attached to it (Fig. 4b), so the specific surface area is the smallest. The nanoparticles on the fiber surface have difficulty aggregating N₂ at low pressure, but when the pressure is increased, the surface MnO₂ nanoparticles can aggregate N₂ in small amounts (Fig. 5a).

As the plasma treatment time was increased from 2 min to 6 min and 10 min, the catalyst showed a typical H3 hysteresis loop (Fig. 5b and c) characteristic of layered aggregates, which was highly consistent with the respective SEM surface morphology of the samples (Fig. 4d and f). The multilayer stacking of MnO₂ nanoparticles resulted in a significant increase in the specific surface area.

At an optimized plasma treatment time of 6 min, the highest specific surface area is up to 8.74 m²/g, which is comparable with an idea specific surface area of 10 m²/g of MnO₂ nanospheres of the same diameter.

In addition, the pore volumes and pore diameters of the different samples are given in Table 1. The sample with a plasma treatment time of 6 min shows the highest specific surface area with the highest pore volume and the smallest pore size.

Table 1
Properties of different synthesized MnO₂@PMIA-t.

	Average size (nm)	Specific surface areas (m ² /g)	Pore Volume (cm ³ /g)	Pore size (nm)
MnO ₂ @PMIA-2	194.30	2.46	0.0039	12.45
MnO ₂ @PMIA-6	130.80	8.74	0.0044	12.24
MnO ₂ @PMIA-10	304.50	7.84	0.0042	27.43

3.3. Catalytic performance of MnO₂@PMIA

To investigate the MnO₂ catalyst loading on the fiber surface after the hydrothermal reaction, TGA tests were carried out on the PMIA under an O₂ atmosphere. As shown in Fig. 6a, the blank PMIA underwent a violent degradation after one complete heating process with a residual weight of 1.03 %. The amount of catalyst in each sample increased with increasing plasma treatment time, in the order of 21.55, 23.08, and 23.54 %.

Fig. 6b shows the DTG curves for pure PMIA and each sample, indicating that the presence of nano-MnO₂ significantly reduces the thermal decomposition temperature of PMIA. The choice of thermally stable PMIA as a substrate can avoid the degradation or carbonization of the fibers in high temperature, high pressure, and strongly oxidizing environments, particularly in hydrothermal experiments.

δ-MnO₂, with its unique interlayer structure that exposes more OV on the surface, can rapidly activate O₂ during the catalytic degradation of formaldehyde, generating large amounts of reactive oxygen species such as -O²⁻/O⁻ [50], thus allowing the reaction to proceed at room temperature without light. The performance of MnO₂@PMIA-t catalyzed degradation of HCHO was tested at room temperature without light by a self-built formaldehyde degradation device.

As shown in Fig. 6c and d, all samples were most rapidly degraded within the first 15 min of the reaction, equilibrating after 30 min. All samples showed activity in the oxidation of HCHO to CO₂ and the rate and amount of CO₂ production was proportional to the extent of HCHO consumption.

The MnO₂@PMIA-2 sample with the smallest specific surface area and the lowest MnO₂ content showed the worst catalytic performance. This sample lost its activity after reaching 74.57 % degradation efficiency for HCHO.

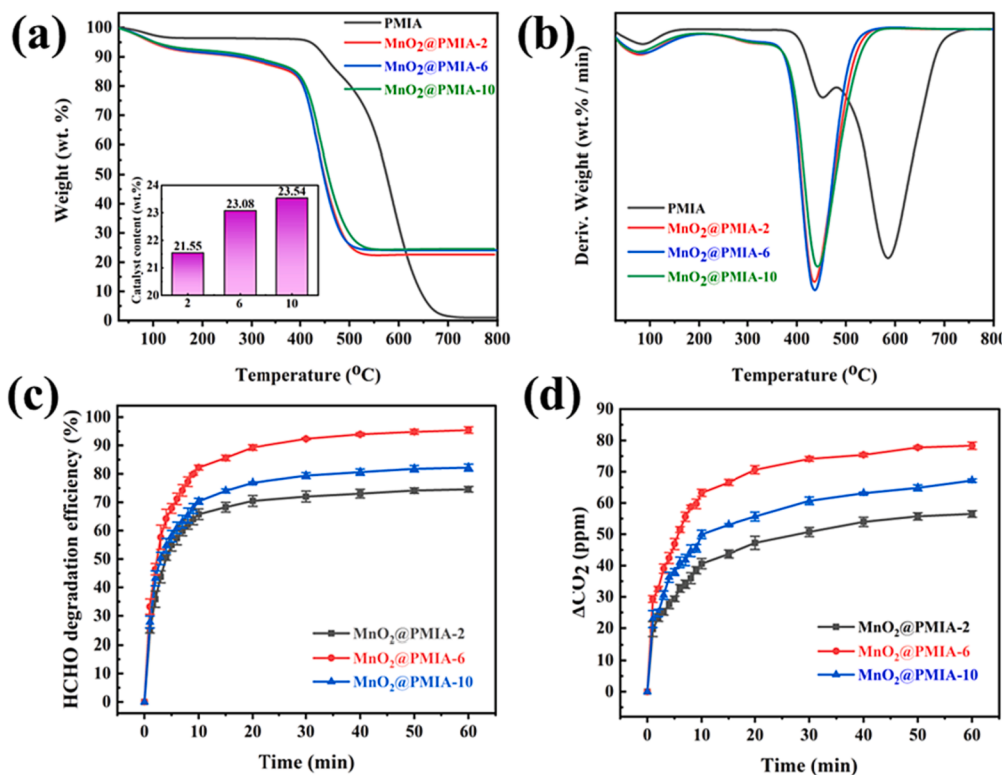


Fig. 6. (a) The TG curves of PMIA and MnO₂@PMIA-t, (b) The DTG curves of PMIA and MnO₂@PMIA-t, (c) HCHO removal test over MnO₂@PMIA-t, (d) Corresponding ΔCO_2 of MnO₂@PMIA-t during HCHO removal test.

MnO₂@PMIA-6 exhibited optimal degradation efficiency due to its high specific surface area and the high loading of MnO₂ nanoparticles on the fiber surface, which fully exposed the surface active sites. The degradation efficiency of HCHO was as high as 95.43 % within 60 min.

Although the catalyst content on the surface of the MnO₂@PMIA-10 sample was the highest, the coating only allowed the exposed nanoparticles on its surface to meet HCHO (decreased specific surface area). The particles in the coating, on the other hand, have difficulty performing the catalytic degradation function due to the difficulty of diffusion contact with formaldehyde. This leads to a decrease in its catalytic performance, which tends to equalize after reaching 82.21 %.

Meanwhile, Fig. S5 demonstrated the catalytic degradation performance of MnO₂@PMIA-B prepared using vitamin B₆ as a reducing agent for formaldehyde under the same test conditions. Its catalytic degradation activity of formaldehyde reached 85.70 % within 60 min, which was much lower than that of MnO₂@PMIA-6.

XRD and FTIR analyses were performed on MnO₂@PMIA-6 after participating in the catalytic degradation of formaldehyde (Fig. S6). After catalytic degradation of formaldehyde, the characteristic peaks appearing in their XRD patterns were still attributed to δ -MnO₂. By analyzing the FTIR spectra of the samples before and after the catalytic degradation of formaldehyde, it was found that the samples involved in the catalytic degradation of formaldehyde produced three consecutive peaks out of 2829–2991 cm⁻¹, which were attributed to the formate species produced after the degradation of formaldehyde.

3.4. Oxygen vacancy regulation mechanism

As mentioned in Section 3.1, the introduction of large amounts of surface –OH and –COOH will allow [MnO₆] to bond with –COOH to release free H⁺, making the near-surface area of the fiber acidic. The acidic conditions will promote the generation of Mn²⁺ by the redox reaction between MnO₄ and –OH. The resulting Mn²⁺ will continue to react with the excess MnO₄ to form more Mn³⁺. The generation of Mn³⁺

will lead to more O atoms escaping from [MnO₆] due to a charge balance to produce more OV, thus significantly improving the room temperature catalytic performance of the MnO₂ nanocatalysts.

We first determined the relative concentrations and oxidation states of the different valence states of Mn and O species by XPS analysis. Fig. 7a shows the XPS spectra of MnO₂@PMIA-2, MnO₂@PMIA-6, and MnO₂@PMIA-10, all of which show characteristic peaks of O and Mn.

O 1 s spectrum (Fig. 7b) was deconvoluted into two peaks at around 529.5 and 531.6 eV [51], which were ascribed to lattice oxygen (O_{latt}) and surface adsorbed oxygen (O_{ads}), respectively. O_{ads} is often used as a quantitative indicator of oxygen adsorption and activation sites on catalyst surfaces so that higher levels of O_{ads} represent greater catalytic activity [52]. The sample with the best catalytic degradation of formaldehyde of all samples, MnO₂@PMIA-6, exhibited the highest O_{ads}/O_{latt} ratio of 0.73.

The Mn 2p signal was deconvoluted into three peaks including 643.0, 641.9, and 640.9 eV (Fig. 7c) which was ascribed to surface Mn⁴⁺, Mn³⁺, and Mn²⁺, respectively [53,54]. The Mn³⁺/(Mn³⁺+Mn⁴⁺) ratios of the samples with plasma treatment durations of 2, 6, and 10 min were 0.38, 0.41, and 0.42, respectively, indicating that the Mn³⁺ concentration in the MnO₂ nanocatalysts increased after hydrothermal growth on the surface of PMIA fibers with extended plasma treatment durations. This is because the introduction of more –OH on the surface of PMIA after plasma treatment makes the conversion of MnO₄ to Mn³⁺ easier and promotes the subsequently formed OV.

In addition, the difference in binding energy (ΔE) obtained from the Mn 3 s (Fig. 7d) measurements, with the average oxidation state (AOS) calculated for each sample based on the empirical equation, AOS = 8.956–1.126 $\times \Delta E$ [55,56]. The AOS of the samples with plasma treatment durations of 2, 6, and 10 min were 3.73, 3.62, and 3.54, respectively. Decreased AOS value along with extended plasma treatment durations furtherly confirmed the previously proposed enhancement mechanism of surface anchored –OH on OV.

XPS tests were performed on MnO₂@PMIA-6 after participating in

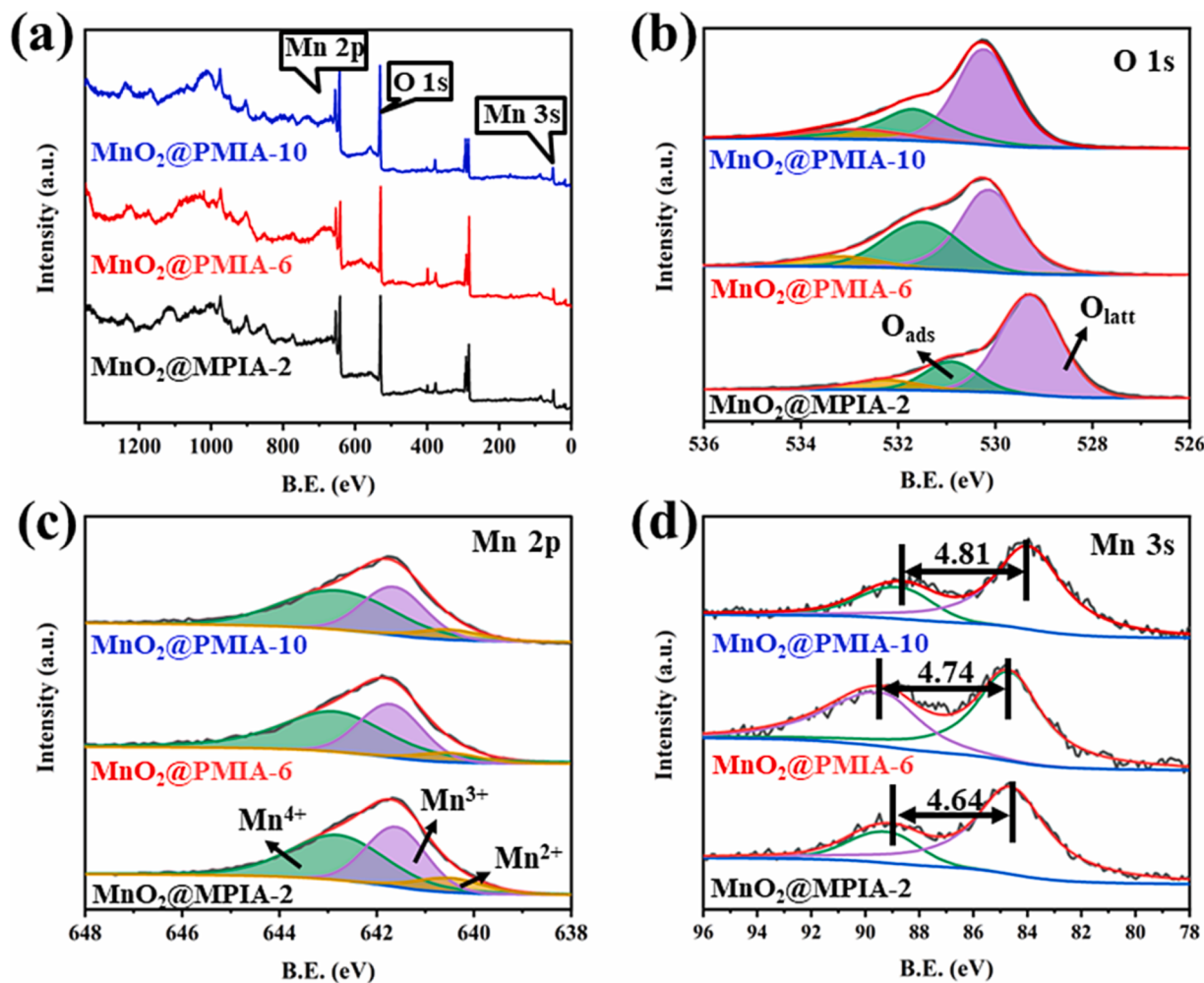


Fig. 7. XPS spectra of $\text{MnO}_2@\text{PMIA-}t$: (a) Survey spectra, (b) O 1 s, (c) Mn 2 p, (d) Mn 3 s.

the catalytic degradation of formaldehyde (Fig. S7), and the experimental results showed that the catalytic degradation of formaldehyde had little effect on the oxidation state of MnO_2 .

In addition, the O 1 s spectra of the $\text{MnO}_2@\text{PMIA-}6$ after its participation in the catalytic degradation of formaldehyde showed a distinct peak at 351 eV, which was attributed to the carbon–oxygen bond (C–O–H) of the formate species formed after the degradation of formaldehyde.

In contrast, the in situ reductive –OH introduced on the PMIA surface by air plasma treatment can confine the reduction reaction to the PMIA surface (Fig. 8b). This facilitates the utilization of reduced species by MnO_2 on the near surface of PMIA to produce more Mn^{3+} , resulting in a higher concentration of OV in MnO_2 on the near surface of PMIA.

The OV concentration obtained by XPS depends on the surface OV concentration. Based on the $\text{O}_{\text{ads}}/\text{O}_{\text{latt}}$ ratio, a ratio of 1:2.81:1.92 can be calculated for the surface OV concentration of various $\text{MnO}_2@\text{PMIA}$ with plasma treatment durations of 2, 6, and 10 min.

The EPR signal intensity, on the other hand, directly responds to the bulk phase OV concentration of the sample. To confirm the effect of different plasma treatment durations on the OV concentration in the bulk phase of MnO_2 , we tested the EPR of samples with different plasma treatment durations. Fig. S9 reveals a g factor of 2.004, which was confirmed as an OV signal as previously reported [57].

As shown in Fig. 8a, all samples exhibited a strong signal caused by the capture of unpaired electrons by OV. As the plasma treatment time increased, the EPR signal of the samples became stronger, indicating an increase in the concentration of OV. The calculated OV concentrations in the bulk phase for plasma treatment durations of 2, 6, and 10 min were

2.80×10^{11} , 3.830×10^{11} , and 4.224×10^{11} spins/ mm^3 respectively, with corresponding ratios of 1:1.37:1.51 (Fig. 8b).

To elucidate the effect of surface anchored reducing –OH versus free –OH in solution on the generation of OV from MnO_2 near the PMIA surface, we compared the results of OV formation between the two in the same hydrothermal environment. Table 2 shows the ratio of $\text{Mn}^{3+}/(\text{Mn}^{3+}+\text{Mn}^{4+})$ and $\text{O}_{\text{ads}}/\text{O}_{\text{latt}}$ calculated from the XPS-measured spectra of each sample (Fig. S8), and OV concentrations calculated from EPR (Fig. S9).

As shown in Table 2, the lowest concentration of Mn^{3+} and OV of $\text{MnO}_2@\text{PMIA-B}$ (free –OH in solution) confirmed that only a small fraction of the free –OH in solution reached the fiber surface, and most generated Mn^{3+} was enveloped by the free $[\text{MnO}_6]$ inside solution instead of on the surface of PMIA fiber.

To further characterize the surface oxygen content of each sample to confirm the relationship between surface OV concentration and plasma treatment duration, H₂-TPR tests were carried out on three samples (the experimental temperature was kept below 400 °C to avoid the influence of the thermal decomposition of the PMIA).

The consumption of H₂ for the samples treated with plasma for 2, 6, and 10 min was 1.007, 1.334, and 1.028 mmol/g respectively (Fig. 8d), which is much higher than the theoretical value of H₂ consumption. According to the TGA analysis (Fig. 6a and b), the presence of MnO_2 lowers the thermal decomposition temperature of PMIA and its thermal decomposition products may consume H₂. Therefore, this test cannot quantify the number of surface-active sites in MnO_2 , but it can be used to compare the relative content of surface-active components of each

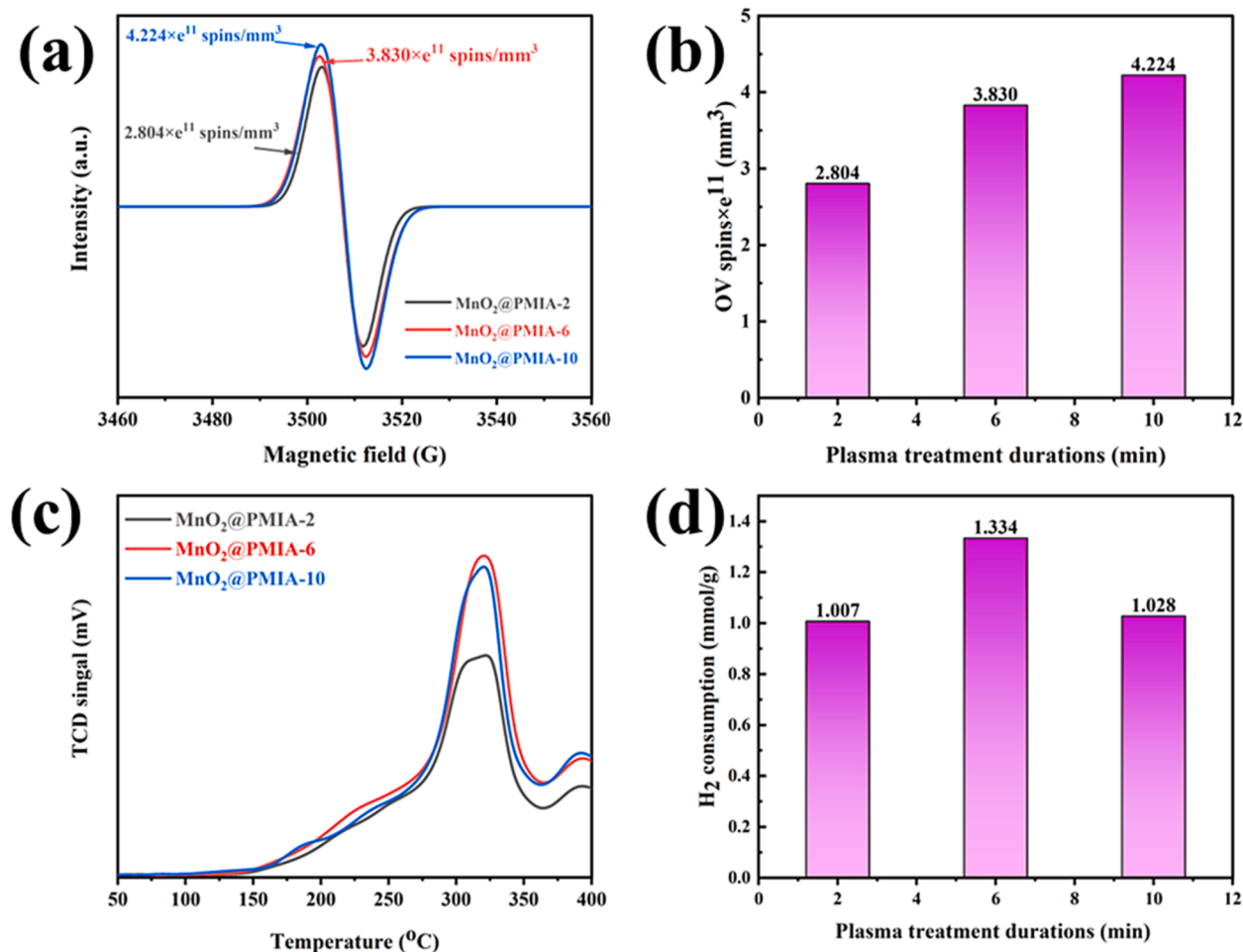


Fig. 8. (a) EPR spectra of MnO₂@PMIA-t, (b) concentrations of OV spins of MnO₂@PMIA – 2, MnO₂@PMIA – 6, and MnO₂@PMIA – 10, (c) H₂-TPR profiles of MnO₂@PMIA-t, (d) H₂ consumption of MnO₂@PMIA – 2, MnO₂@PMIA – 6, and MnO₂@PMIA – 10.

Table 2

The ratio of Mn³⁺/(Mn³⁺+Mn⁴⁺), O_{ads}/O_{latt}, and OV concentrations of MnO₂@PMIA-t and MnO₂@PMIA-B.

Molecular ratio Mn ³⁺ / (Mn ³⁺ +Mn ⁴⁺)	Molecular ratio O _{ads} /O _{latt}	OV concentrations (spins/mm ³)
MnO ₂ @PMIA-2	0.38	2.80 × 10 ¹¹
MnO ₂ @PMIA-6	0.41	3.83 × 10 ¹¹
MnO ₂ @PMIA- 10	0.42	4.22 × 10 ¹¹
MnO ₂ @PMIA-B	0.29	1.39 × 10 ¹¹

sample horizontally.

As the temperature increases, the amount of O_{ads} first begins to decrease and higher temperatures cause the amount of O_{latt} to begin to decrease as well.

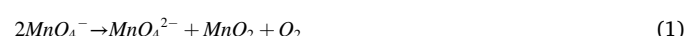
MnO₂@PMIA-6 showed the highest surface weakly bound oxygen, as shown in Fig. 8c, where the consumption of H₂ up to 270 °C was attributed to the weakly bound O_{ads} on the sample surface. The consumption of H₂ by all samples peaked when the temperature was increased to 320 °C. The peak intensity of MnO₂@PMIA-6 was the highest of all samples because it had the highest specific surface area and the highest OV content, resulting in more surface O_{latt} and therefore more H₂ consumption than the other samples.

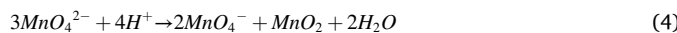
The above experimental results demonstrate that the concentration of both bulk phase and surface OV in MnO₂@PMIA can be effectively regulated by modulating the in situ reduced –OH on the fiber surface

introduced by plasma treatment. Unlike surface OV which directly converts surface-adsorbed oxygen into highly catalytically active oxygen active species, bulk phase OV increases the catalytic activity of the catalyst by reducing the catalyst band gap to increase the carrier concentration [21]. The effect of surface OV concentration on the catalytic performance of non-homogeneous catalysts has been reported to be much higher than that of bulk phase OV [58]. In contrast, the bulk phase OV of MnO₂@PMIA-6, although slightly lower than that of MnO₂@PMIA-10, has a significantly higher surface OV. This is the reason why MnO₂@PMIA-6 exhibits the strongest catalytic activity.

Based on the above experimental results, we proposed the following hydrothermal growth mechanism for MnO₂ (Equations (1) to (4)).

- (1) Under heating conditions, MnO₄⁻ in an aqueous solution is readily reduced to MnO₂.
- (2) As a result of the plasma treatment, large amounts of –OH and –COOH were introduced and the bonding of [MnO₆] to –COOH led to the detachment of H⁺, making the near-surface region of the fibers acidic and facilitating the redox reaction of MnO₄⁻ with –OH to produce Mn²⁺.
- (3) Mn²⁺ will continue to react with MnO₄⁻ to give Mn³⁺ and MnO₄²⁻.
- (4) As the reaction proceeds, MnO₄²⁻ is also converted to MnO₂.





Here, R indicates the PMIA fibers.

The reduction of Mn^{4+} to Mn^{3+} in the $[\text{MnO}_6]$ lattice leads to more oxygen detachment and more OV production [59,60]. In contrast, the active $-\text{OH}$ on the surface of PMIA fibers acts as an in situ reducing agent, which allows the formation of Mn^{3+} to be confined to the chemically bonded $[\text{MnO}_6]$ on the fiber surface (by $-\text{COOH}$ from both plasma treatment and $-\text{OH}$ oxidation), rather than growing free in solution. This unique growth method allows the final PMIA fiber-based MnO_2 nanocatalysts to be obtained with abundant OV.

3.5. Laundering durability

Laundering durability means that MnO_x and PMIA stay physically integrated after washing with water. Poor laundering durability to washing is one of the key reasons preventing the practical application of fiber-based MnO_2 nanocatalysts. The plasma introduction of $-\text{COOH}$, i.e., the oxidation of the introduced $-\text{OH}$, provides many bondable chemical sites between the fiber and the MnO_2 nanocatalysts (Fig. S10). It can be expected that fiber-based MnO_2 nanocatalysts prepared by plasma-modulated PMIA with surface $-\text{OH}$ and $-\text{COOH}$ by the hydrothermal method will possess good catalytic activity even after laundering.

$\text{MnO}_2@\text{PMIA-6}$ and $\text{MnO}_2@\text{PMIA-0}$ were selected for accelerated laundering tests for laundering durability tests (one accelerated wash equals 5 domestic or commercial washes) according to the AATCC Test Method 61–2003. Notably, after washed by laundering machine, a home laundering using pure water was further performed to ensure the completely remove of detergent, which can be confirmed by Fig. S11.

As shown in Fig. 9a, after four accelerated laundering cycles (equal to 20 household laundering cycles), $\text{MnO}_2@\text{PMIA-6}$ showed only 0.94 % loss in the mass of MnO_2 , indicating strong bonds between the MnO_2 nanoparticles and the fibers and less susceptibility to powder loss. In contrast, the wash fastness of $\text{MnO}_2@\text{PMIA-0}$ (without plasma treatment) was very poor, with a 65.03 % mass loss of the MnO_2 after four accelerated laundering cycles. This is due to the purely physical interaction between MnO_2 nanoparticles and PMIA and the lack of chemical bonding. The experimental results demonstrate that the introduction of carboxyl groups on the fiber surface by air plasma treatment can significantly improve its fastness of washing.

In addition, catalytic regeneration experiments were performed on the samples after four accelerated laundering cycles. The samples that had lost their catalytic activity were treated in an oven at 110 °C for 2 h and then subjected to catalytic degradation of HCHO again. The results

of the HCHO degradation experiments are shown in Fig. 9b. After 4 accelerated laundering cycles and 4 regeneration cycles, the catalytic degradation efficiency of the $\text{MnO}_2@\text{PMIA-6}$ sample did not decrease significantly and remained at 90.97 % (only 4.46 % loss in catalytic activity).

The above experimental results confirm that the synergistic introduction of $-\text{OH}$ and $-\text{COOH}$ on the surface of PMIA fibers can effectively enhance the fastness of the bond between PMIA fibers and MnO_2 while maintaining a high catalytic degradation of formaldehyde in its multiple cycles.

4. Conclusions

It was still a long way to the practical application of fiber-based MnO_2 nanocatalysts which show high practical potential due to thereof significantly reduced specific surface area, catalytic performance, and poor laundering durability.

In this work, surface anchored $-\text{OH}$ and $-\text{COOH}$ on PMIA were finely regulated by varying the plasma treatment durations from 0 to 10 mins. $-\text{OH}$ plays as a reduction agent to facilitate the production of Mn^{3+} close to the PMIA surface and thus promote subsequent output of oxygen vacancy (OV) during hydrothermal reactions. The plasma introduced and $-\text{OH}$ oxidized $-\text{COOH}$ acted together as multiple binding sites to bridge the MnO_2 catalyst and PMIA fiber, which endows the $\text{MnO}_2@\text{PMIA}$ excellent laundering durability evidenced by the almost unchanged catalytic performance targeting formaldehyde (high up to 90.97 %) even after 20 home laundering cycles. The mechanism of modulation of oxygen vacancy, specific surface area, and water fastness by in situ $-\text{OH}$ and $-\text{COOH}$ on the relevant surfaces is proposed and confirmed by FTIR, XPS, SEM, and BET. $\text{MnO}_2@\text{PMIA-6}$ shows the best comprehensive catalytic performance with 95.43 % removal efficiency targeting formaldehyde at room temperature for 60 min.

CRediT authorship contribution statement

Zijian Duan: Methodology, Formal analysis, Writing – original draft. **Yahui Zhou:** Validation, Investigation. **Huiyu Yang:** Validation, Investigation. **Dali Yan:** Validation, Investigation. **Dengpeng Song:** Validation, Investigation. **Hao Liu:** Validation, Investigation. **Bo Deng:** Conceptualization, Resources, Writing – review & editing, Supervision. **Shuai Peng:** Supervision. **Weilin Xu:** Supervision, Funding acquisition.

Declaration of Competing Interest

The authors declare that they have no known competing financial

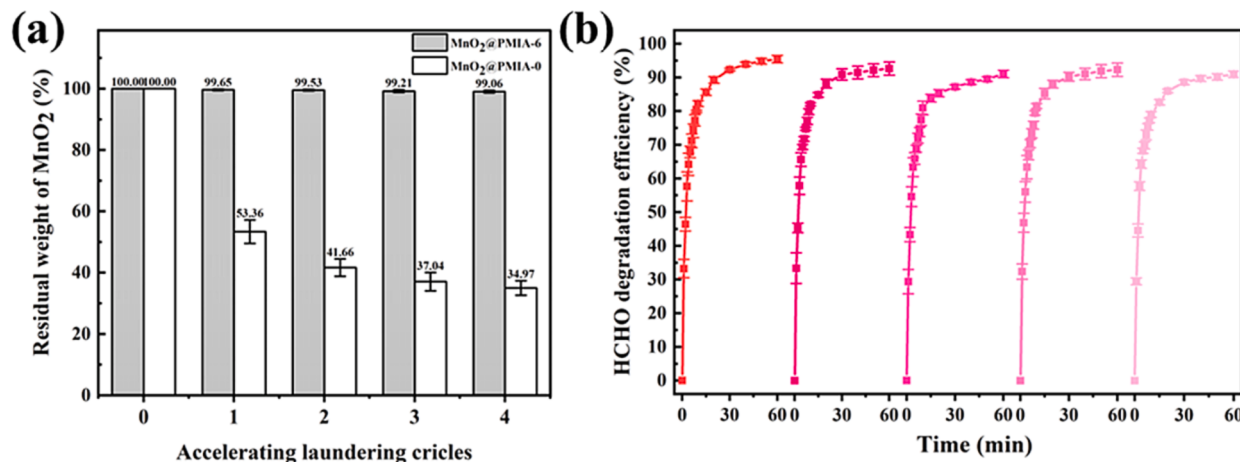


Fig. 9. (a) Laundering durability test of $\text{MnO}_2@\text{PMIA-6}$ and $\text{MnO}_2@\text{PMIA-0}$, (b) Catalytic performance of $\text{MnO}_2@\text{PMIA-6}$ after multiple accelerated laundering cycles.

interests or personal relationships that could have appeared to influence the work reported in this paper.

Data availability

Data will be made available on request.

Acknowledgments

This work was supported by the National Natural Science Foundation of China (No. U21A2095), The Key Research and Development Program of Hubei Province (No. 2021BAA068), The Department of Education of Guangdong Province (2019GZDXM006) and the Foundation of State Key Laboratory of Coal Combustion (FSKLCCA2109).

Appendix A. Supplementary data

Supplementary data to this article can be found online at <https://doi.org/10.1016/j.cej.2023.145104>.

References

- [1] V.K. Pal, A.J. Li, H.K. Zhu, K. Kannan, Diurnal variability in urinary volatile organic compound metabolites and its association with oxidative stress biomarkers, *Sci. Total Environ.* 818 (2022) 9.
- [2] A. Lamplugh, M. Harries, F. Xiang, J. Trinh, A. Hecobian, L.D. Montoya, Occupational exposure to volatile organic compounds and health risks in Colorado nail salons, *Environ. Pollut.* 249 (2019) 518–526.
- [3] W. Zhang, G. Li, H. Liu, J. Chen, S. Ma, M. Wen, J. Kong, T. An, Photocatalytic degradation mechanism of gaseous styrene over Au/TiO₂/CNTs: relevance of superficial state with deactivation mechanism, *Appl. Catal. B-Environ.* 272 (2020) 118969.
- [4] Z. Dai, J. Su, X. Zhu, K. Xu, J. Zhu, C. Huang, Q. Ke, Multifunctional polyethylene (PE)/polypropylene (PP) bicomponent fiber filter with anchored nanocrystalline MnO₂ for effective air purification, *J. Mater. Chem. A* 6 (30) (2018) 14856–14866.
- [5] S. Yang, Z. Qi, Y. Wen, X. Wang, S. Zhang, W. Li, S. Li, Generation of abundant oxygen vacancies in Fe doped δ -MnO₂ by a facile interfacial synthesis strategy for highly efficient catalysis of VOCs oxidation, *Chem. Eng. J.* 452 (2023) 139657.
- [6] M. Hakim, Y.Y. Broza, O. Barash, N. Peled, M. Phillips, A. Amann, H. Haick, Volatile Organic Compounds of Lung Cancer and Possible Biochemical Pathways, *Chem. Rev.* 112 (2012) 5949.
- [7] J. Ban, W.J. Su, Y. Zhong, C. Liu, T.T. Li, Ambient formaldehyde and mortality: A time series analysis in China, *Sci. Adv.* 8 (2022) 8.
- [8] Y. Xu, J. Dhainaut, G. Rochard, J.P. Daquin, A.S. Mamede, J.M. Giraudon, J. F. Lamonié, H. Zhang, S. Royer, Hierarchical porous epsilon-MnO₂ from perovskite precursor: Application to the formaldehyde total oxidation, *Chem. Eng. J.* 388 (2020) 12.
- [9] W.X. Zhang, M. Xue, J. Fan, L.L. Qiu, W.X. Zheng, Y.Y. Liu, Z.H. Meng, Flory-Huggins VOC Photonics Sensor Made of Cellulose Derivatives, *ACS Appl. Mater. Interfaces* 14 (2022) 10701–10711.
- [10] S. Peng, X.X. Yang, J. Strong, B. Sarkar, Q. Jiang, F. Peng, D.F. Liu, H.L. Wang, MnO₂-decorated N-doped carbon nanotube with boosted activity for low-temperature oxidation of formaldehyde, *J. Hazard. Mater.* 396 (2020) 10.
- [11] W.J. Wang, F.W. Lin, T.C. An, S.X. Qiu, H.D. Yu, B.B. Yan, G.Y. Chen, L.A. Hou, Photocatalytic mineralization of indoor VOC mixtures over unique ternary TiO₂/C/MnO₂ with high adsorption selectivity, *Chem. Eng. J.*, 425 (2022) 131678.
- [12] D.Y. Chen, G.P. Zhang, M.M. Wang, N.J. Li, Q.F. Xu, H. Li, J.H. He, J.M. Lu, Pt/MnO₂ Nanoflowers Anchored to Boron Nitride Aerogels for Highly Efficient Enrichment and Catalytic Oxidation of Formaldehyde at Room Temperature, *Angew. Chem.-Int. Edit.* 60 (2021) 6377–6381.
- [13] E.C. Gillispie, R.E. Austin, N.A. Rivera, R. Bolich, O.W. Duckworth, P. Bradley, A. Amoozegar, D. Hesterberg, M.L. Polizzotto, Soil Weathering as an Engine for Manganese Contamination of Well Water, *Environ. Sci. Technol.* 50 (2016) 9963–9971.
- [14] S.P. Rong, P.Y. Zhang, J.L. Wang, F. Liu, Y.J. Yang, G.L. Yang, S. Liu, Ultrathin manganese dioxide nanosheets for formaldehyde removal and regeneration performance, *Chem. Eng. J.* 306 (2016) 1172–1179.
- [15] A. Hazarika, B.K. Deka, K. Kong, D. Kim, Y.W. Nam, J.H. Choi, C.G. Kim, Y.B. Park, H.W. Park, Microwave absorption and mechanical performance of alpha-MnO₂ nanostructures grown on woven Kevlar fiber/reduced graphene oxide-polyaniline nanofiber array-reinforced polyester resin composites, *Compos. Pt. B-Eng.* 140 (2018) 123–132.
- [16] B.B. Chen, B. Wu, L.M. Yu, M. Crocker, C. Shi, Investigation into the Catalytic Roles of Various Oxygen Species over Different Crystal Phases of MnO₂ for C₆H₆ and HCHO Oxidation, *ACS Catal.* 10 (2020) 6176–6187.
- [17] X.R. Liang, J.E. Post, B. Lanson, X.M. Wang, M.Q. Zhu, F. Liu, W.F. Tan, X.H. Feng, G.M. Zhu, X. Zhang, J.J. De Yoreo, Coupled morphological and structural evolution of delta-MnO₂ to alpha-MnO₂ through multistage oriented assembly processes: the role of Mn(III), *Environ. Sci.-Nano* 7 (2020) 238–249.
- [18] J.W. Ye, M.H. Zhou, Y. Le, B. Cheng, J.G. Yu, Three-dimensional carbon foam supported MnO₂/Pt for rapid capture and catalytic oxidation of formaldehyde at room temperature, *Appl. Catal. B-Environ.* 267 (2020) 8.
- [19] Z.M. Zhang, L. Xiang, F.W. Lin, Z. Wang, B.B. Yan, G.Y. Chen, Catalytic deep degradation of Cl-VOCs with the assistance of ozone at low temperature over MnO₂ catalysts, *Chem. Eng. J.*, 426 (2021) 130814.
- [20] J.Y. Zheng, K.L. Zhou, W.K. Zhao, Y.S. Wang, J.D. He, X.X. Wang, H. Wang, H. Yan, C.B. Han, Enhanced the synergistic degradation effect between active hydroxyl and reactive oxygen species for indoor formaldehyde based on platinum atoms modified MnOOH/MnO₂ catalyst, *J. Colloid Interface Sci.* 628 (2022) 359–370.
- [21] L.i. Li, X. Feng, Y. Nie, S. Chen, F. Shi, K. Xiong, W. Ding, X. Qi, J. Hu, Z. Wei, L.-J. Wan, M. Xia, Insight into the Effect of Oxygen Vacancy Concentration on the Catalytic Performance of MnO₂, *ACS Catal.* 5 (8) (2015) 4825–4832.
- [22] S. Lee, G. Nam, J. Sun, J.S. Lee, H.W. Lee, W. Chen, J. Cho, Y. Cui, Enhanced Intrinsic Catalytic Activity of lambda-MnO₂ by Electrochemical Tuning and Oxygen Vacancy Generation, *Angew. Chem.-Int. Edit.* 55 (2016) 8599–8604.
- [23] W. Hong, M.P. Shau, T.L. Zhu, H.N. Wang, Y. Sun, F.X. Shen, X. Li, To Promote Ozone Catalytic Decomposition by Fabricating Manganese Vacancies in epsilon-MnO₂ Catalyst via Selective Dissolution of Mn-Li Precursors, *Appl. Catal. B-Environ.* 274 (2020) 13.
- [24] I. Fernandez-Olmo, P. Mantecón, B. Markiv, L. Ruiz-Azcona, M. Santibanez, A Review on the Environmental Exposure to Airborne Manganese, Biomonitoring, and Neurological/Neuropsychological Outcomes, *Rev. Environ. Contam. Toxicol.*, Cham 254 (2021) 85–130.
- [25] M. Arora, A. Bradman, C. Austin, M. Vedar, N. Holland, B. Eskenazi, D.R. Smith, Determining Fetal Manganese Exposure from Mantle Dentine of Deciduous Teeth, *Environ. Sci. Technol.* 46 (9) (2012) 5118–5125.
- [26] S.P. Rong, P.Y. Zhang, F. Liu, Y.J. Yang, Engineering Crystal Facet of alpha-MnO₂ Nanowire for Highly Efficient Catalytic Oxidation of Carcinogenic Airborne Formaldehyde, *ACS Catal.* 8 (2018) 3435–3446.
- [27] Z. Dai, J. Zhu, J. Yan, J. Su, Y. Gao, X. Zhang, Q. Ke, G.N. Parsons, An Advanced Dual-Function MnO₂-Fabric Air Filter Combining Catalytic Oxidation of Formaldehyde and High-Efficiency Fine Particulate Matter Removal, *Adv. Funct. Mater.* 30 (42) (2020) 2001488.
- [28] D. Wei, J. Liu, Z. Luo, X. Xie, Insight into the reactions of antimonite with manganese oxides: Synergistic effects of Mn(III) and oxygen vacancies, *Water Res.* 232 (2023) 119681.
- [29] M. Hu, L.H. Yin, H.X. Zhou, L.X. Wu, K. Yuan, B. Pan, Z.X. Zhong, W.H. Xing, Manganese dioxide-filled hierarchical porous nanofiber membrane for indoor air cleaning at room temperature, *J. Membr. Sci.* 605 (2020) 9.
- [30] F. Liu, S.P. Rong, P.Y. Zhang, L.L. Gao, One-step synthesis of nanocarbon-decorated MnO₂ with superior activity for indoor formaldehyde removal at room temperature, *Appl. Catal. B-Environ.* 235 (2018) 158–167.
- [31] J.W. Chen, H.Y. Tang, M. Huang, Y. Yan, J. Zhang, H.G. Liu, J. Zhang, G. Wang, R. L. Wang, Surface Lattice Oxygen Activation by Nitrogen-Doped Manganese Dioxide as an Effective and Longevous Catalyst for Indoor HCHO Decomposition, *ACS Appl. Mater. Interfaces* 13 (2021) 26960–26970.
- [32] J.L. Wang, J.E. Li, C.J. Jiang, P. Zhou, P.Y. Zhang, J.G. Yu, The effect of manganese vacancy in birnessite-type MnO₂ on room-temperature oxidation of formaldehyde in air, *Appl. Catal. B-Environ.* 204 (2017) 147–155.
- [33] Y. Huang, Y. Liu, W. Wang, M.J. Chen, H.W. Li, S.C. Lee, W.K. Ho, T.T. Huang, J. J. Cao, Oxygen vacancy-engineered delta-MnO_x/activated carbon for room-temperature catalytic oxidation of formaldehyde, *Appl. Catal. B-Environ.* 278 (2020) 9.
- [34] J. Han, D.S. Li, L. Jiang, D.N. Fang, Co-MnO₂ Nanorods for High-Performance Sodium/Potassium-Ion Batteries and Highly Conductive Gel-Type Supercapacitors, *Adv. Sci.* 2022 (9) (2022) 2105510.
- [35] S.P. Mo, Q. Zhang, J.Q. Li, Y.H. Sun, Q.M. Ren, S.B. Zou, Q. Zhang, J.H. Lu, M. L. Fu, D.Q. Mo, J.L. Wu, H.M. Huang, D.Q. Ye, Highly Efficient Mesoporous MnO₂ Catalysts for the Total Toluene Oxidation: Oxygen-Vacancy Defect Engineering and Involved Intermediates Using In Situ DRIFTS, *Appl. Catal. B-Environ.* 264 (2020), 118464.
- [36] Z. Xiong, J. Huang, Y.Z. Wu, X. Gong, Robust multifunctional fluorine-free superhydrophobic fabrics for high-efficiency oil-water separation with ultrahigh flux, *Nanoscale* 17 (2022) 5840–5850.
- [37] F.X. Chen, H.Y. Yang, K. Li, B. Deng, Q.S. Li, X. Liu, B.H. Dong, X.F. Xiao, D. Wang, Y. Qin, S.M. Wang, K.Q. Zhang, W.L. Xu, Facile and Effective Coloration of Dye-Inert Carbon Fiber Fabrics with Tunable Colours and Excellent Laundering Durability, *ACS Nano* 11 (2017) 10330–10336.
- [38] Z.H. Liu, Y.P. Luo, X.M. Zhao, K.Y. Zheng, M.H. Wu, L.L. Wang, A natural antibacterial agent based on modified chitosan by hinokitiol for antibacterial application on cotton fabric, *Cellulose* 27 (2022) 2731–2742.
- [39] B. Deng, R. Cai, Y. Yu, H.Q. Jiang, C.L. Wang, J. Li, L.F. Li, Y.u. Ming, J.Y. Li, L. D. Xie, Q. Huang, C.H. Fan, Laundering Durability of Superhydrophobic Cotton Fabric, *Adv. Mater.* 2010 (22) (2010) 5473–5477.
- [40] R.L. Kovacs, M. Csontos, S. Gyongyosi, J. Elek, B. Parditka, G. Deak, A. Kuki, S. Keki, Z. Erdelyi, Surface characterization of plasma-modified low density polyethylene by attenuated total reflectance fourier-transform infrared (ATR-FTIR) spectroscopy combined with chemometrics, *Polym. Test* 96 (2021) 8.
- [41] R. Molina, R. Bitar, P. Cools, R. Morent, N. De Geyter, Effect of liquid impregnation on DBD atmospheric pressure plasma treatment of cotton, *Cellulose* 27 (2020) 7847–7859.
- [42] E. Bozaci, K. Sever, M. Sarikanat, Y. Seki, A. Demir, E. Ozdogan, I. Tavman, Effects of the atmospheric plasma treatments on surface and mechanical properties of flax fiber and adhesion between fiber-matrix for composite materials, *Compos. Pt. B-Eng.* 45 (2013) 565–572.

- [43] T. Wang, X.P. He, Y. Li, J.D. Li, Novel poly(piperazine-amide) (PA) nanofiltration membrane based poly(m-phenylene isophthalamide) (PMIA) hollow fiber substrate for treatment of dye solutions, *Chem. Eng. J.* 351 (2018) 1013–1026.
- [44] Z. Li, X.D. Cheng, S. He, X.J. Shi, L.L. Gong, H.P. Zhang, Aramid fibers reinforced silica aerogel composites with low thermal conductivity and improved mechanical performance, *Compos. Pt. A-Appl. Sci. Manuf.* 84 (2016) 316–325.
- [45] C.X. Jia, P. Chen, B. Li, Q.A. Wang, C. Lu, Q. Yu, Effects of Twaron fiber surface treatment by air dielectric barrier discharge plasma on the interfacial adhesion in fiber reinforced composites, *Surf. Coat. Technol.* 204 (2010) 3668–3675.
- [46] V. Jirásek, Š. Stehlík, P. Štenclová, A. Artemenko, B. Rezek, A. Kromka, Hydroxylation and self-assembly of colloidal hydrogenated nanodiamonds by aqueous oxygen radicals from atmospheric pressure plasma jet, *RSC Adv.* 8 (66) (2018) 37681–37692.
- [47] A. Fahmy, R. Mix, A. Schönhals, J.F. Friedrich, Structure of Plasma-Deposited Poly(acrylic acid) Films, *Plasma Process. Polym.* 8 (2) (2011) 147–159.
- [48] V.B.R. Boppana, S. Yusuf, G.S. Hutchings, F. Jiao, Nanostructured Alkaline-Cation-Containing-MnO₂ for Photocatalytic Water Oxidation, *Adv. Funct. Mater.* 23 (2013) 878–884.
- [49] Y. Liu, Y. Qiao, W.X. Zhang, H. Wang, K.Y. Chen, H.P. Zhu, Z. Li, Y.H. Huang, Nanostructured alkali cation incorporated delta-MnO₂ cathode materials for aqueous sodium-ion batteries, *J. Mater. Chem. A* 3 (2015) 7780–7785.
- [50] C. Dong, Z.P. Qu, X. Jiang, Y.W. Ren, Tuning oxygen vacancy concentration of MnO₂ through metal doping for improved toluene oxidation, *J. Hazard. Mater.* 391 (2020) 13.
- [51] R.N. Yang, S.M. Peng, B. Lan, M. Sun, Z.H. Zhou, C.Y. Sun, Z.H. Gao, G.C.A. Xing, L. Yu, Oxygen Defect Engineering of beta-MnO₂ Catalysts via Phase Transformation for Selective Catalytic Reduction of NO, *Small* 17 (2021) 13.
- [52] G. Yan, Y. Lian, Y. Gu, C. Yang, H. Sun, Q. Mu, Q. Li, W. Zhu, X. Zheng, M. Chen, J. Zhu, Z. Deng, Y. Peng, Phase and Morphology Transformation of MnO₂ Induced by Ionic Liquids toward Efficient Water Oxidation, *ACS Catal.* 8 (11) (2018) 10137–10147.
- [53] Y. Lyu, C.T. Li, X.Y. Du, Y.C. Zhu, Y.D. Zhang, S.H. Li, Catalytic oxidation of toluene over MnO₂ catalysts with different Mn (II) precursors and the study of reaction pathway, *Fuel* 262 (2020) 9.
- [54] Y. Cao, W. Sun, C. Guo, L.u. Zheng, M. Yao, Y. Wang, Rational Construction of Yolk-Shell Bimetal-Modified Quinonyl-Rich Covalent Organic Polymers with Ultralong Lithium-Storage Mechanism, *ACS Nano* 16 (6) (2022) 9830–9842.
- [55] E.S. Ilton, J.E. Post, P.J. Heaney, F.T. Ling, S.N. Kerisit, XPS determination of Mn oxidation states in Mn (hydr)oxides, *Appl. Surf. Sci.* 366 (2016) 475–485.
- [56] D. Chlala, J.M. Giraudon, N. Nuns, C. Lancelot, R.N. Vannier, M. Labaki, J. F. Lamonier, Active Mn species well dispersed on Ca²⁺ enriched apatite for total oxidation of toluene, *Appl. Catal. B-Environ.* 184 (2016) 87–95.
- [57] Y.T. Wang, J.M. Cai, M.Q. Wu, J.H. Chen, W.Y. Zhao, Y. Tian, T. Ding, J. Zhang, Z. Jiang, X.G. Li, Rational Construction of Oxygen Vacancies onto Tungsten Trioxide to Improve Visible Light Photocatalytic Water Oxidation Reaction, *Appl. Catal. B-Environ.* 239 (2018) 398–407.
- [58] A. Zhang, R. Gao, L. Hu, X. Zang, R.u. Yang, S. Wang, S. Yao, Z. Yang, H. Hao, Y.-M. Yan, Rich bulk oxygen Vacancies-Engineered MnO₂ with enhanced charge transfer kinetics for supercapacitor, *Chem. Eng. J.* 417 (2021) 129186.
- [59] Z.Q. Wang, H.Z. Jia, T. Zheng, Y.C. Dai, C. Zhang, X.T. Guo, T.C. Wang, L.Y. Zhu, Promoted catalytic transformation of polycyclic aromatic hydrocarbons by MnO₂ polymorphs: Synergistic effects of Mn³⁺ and oxygen vacancies, *Appl. Catal. B-Environ.* 272 (2020) 9.
- [60] C. Dong, Z.W. Liu, J.Y. Liu, W.C. Wang, L. Cui, R.C. Luo, H.L. Guo, X.L. Zheng, S. Qiao, X.W. Du, J. Yang, Modest Oxygen-Defective Amorphous Manganese-Based Nanoparticle Mullite with Superior Overall Electrocatalytic Performance for Oxygen Reduction Reaction, *Small* 13 (2017) 9.